Insight into the intrinsic mechanism of improving electrochemical performance via constructing the preferred crystal orientation in lithium cobalt dioxide

Yue Chen,[a,b] ⊥ Yubiao Niu,[b] ⊥ Chun Lin,[a,c] Jiaxin Li,[a,d] * Yingbin Lin,[a,c] GuiGui Xu,[a] Richard E. Palmer,[b] and Zhigao Huang [a,d] *

[a.] *College of Physics and Energy, Fujian Normal University, Fujian Provincial Key Laboratory of Quantum Manipulation and New Energy Materials, Fuzhou，350117, China*

[b.] *College of Engineering, Swansea University, Bay Campus, Swansea, SA1 8EN, UK.*

[c.] *Fujian Provincial Engineering Technical Research Centre of Solar-Energy Conversion and Stored Energy, Fuzhou，350117, China*

[d.] *Fujian Provincial Collaborative Innovation Centre for Advanced High-Field Superconducting Materials and Engineering, Fuzhou, 350117, China*

E-mail: ljx0721@qq.com, zghuang@fjnu.edu.cn;

Abstract

Surface properties of cathode materials play important roles in the transport of lithium-ions/electrons and the formation of surface passivation layer. Optimizing the exposed crystal facets of cathode materials can promote the diffusion of lithium-ions and enhance cathode surface stability, which may ultimately dominate cathode's performance and stability in lithium-ion batteries. Here, polycrystalline $LiCoO_2$ (LCO) thin films with (0003) and $\{10\bar{1}1\}$ preferred orientations were prepared as the well-defined model electrodes. *In situ* Current-Sensing Atomic Force Microscopy (CSAFM) was employed to investigate the lithium de-intercalation and electronic conductivity evolution of the (0003) and $\{10\bar{1}1\}$ facts in organic electrolyte at the nanoscale. It was found that the lithium deintercalation following a "Li-rich core model" in the LCO grains, and the LCO grains with (0003) crystal face show less conductivity than those with $\{10\bar{1}1\}$ faces. Moreover, X-ray photoelectron spectroscopy characterization of the charged electrode surface indicates that a denser surface passivation layer is formed on $\{10\bar{1}1\}$ than that on (0003) crystal faces. This is caused by the lower adsorption energy of decomposition molecule on $\{10\bar{1}1\}$ crystal faces and higher work function (due to the surface atomic structure) for $\{10\bar{1}1\}$ crystal faces, as confirmed by Density Functional Theory (DFT) and Kelvin probe force microscopy (KPFM) results. In addition, electrochemical measurements confirm that the thin film electrodes with $\{10\bar{1}1\}$ preferred orientation not only show smaller electrode polarization, but also more readily form a stable surface passivation layer compared with the (0003) preferred orientation. This work highlights the importance of cathode surface conductivity, and also suggests that the $\{10\bar{1}1\}$ facet atomic structure may thermodynamically promote the physical/chemical adsorption and decomposition of electrolyte.

KEYWORDS

Lithium batteries; $LiCoO_2$ thin-film electrode; Interface/surface compatibility; In situ Current-Sensing AFM

1. Introduction

High energy density and power density are two pervasive and persistent concerns in lithium-ion batteries. Increasing the working voltage and charging rate of cathode materials are two effective strategies [1-2], but they are usually limited by the cathode surface stability and electronic/lithium transport, respectively. Therefore, the understanding of electronic/lithium conductivity and surface passivation layer in cathode materials is essential for its practical application and development. Since the most widely used layered lithium transition metal oxides ($Li_{1+x}M_{1-x}O_2$, M = Ni, Mn, Co) show distinctive anisotropic physical/chemical properties [3], in-depth studies of the cathode surface stability and electronic/lithium conductivity on different crystal faces are therefore highly needed.

Many efforts have been done to study the anisotropic lithium migration in lithium cobalt oxide (LCO) thin film with different preferred orientations [4-7]. Dellen et al. studied the lithium de-/intercalation in the LCO thin films with (0003) preferred orientation, and it was found that the pinning of Li-ions may create cracks along [00l] direction which decreases the battery reversible capacity [4, 5]. Haiyan et al. reported that LCO (10$\bar{1}$4) oriented thin film provides a higher Li-ion diffusion coefficient (7×10^{-10} cm^2/s) compared with (0003) oriented films (8×10^{-11} cm^2/s) [6]. Moreover, due to the easily accessible Li-ion diffusion channels, LCO thin films with (11$\bar{2}$0) preferred orientation were also found to show 20 % more capacity than that with (0003) orientation at 10 C charge/discharge rate [7]. It is well known that, in the battery charge/discharge process, both lithium ions and electrons shuttle back and forth within the host lattice of cathode materials [8, 9]. Therefore, the Li ion migration and electronic conductivity are equally important to the battery performances. However, the differences in electrode performances were merely attributed to the anisotropy of Li-ion migration in these studies. As for the lithium deintercalation induced electronic conductivity changes and surface physicochemical properties of LCO thin film with certain preferred orientation have hardly been discussed.

The electronic conductivity of electrode materials directly determines the polarization status of lithium-ion batteries, and further influences the battery high-rate performance. With the decrease of Li contents (x) in Li_xCoO_2, an insulator-to-metal transition (IMT) was observed, resulting from the transition of insulated O3-I phase to the metallic O3-II phase [10-12]. This implies that the Li-rich $Li_{1-0.9}CoO_2$ is insulated while the Li-poor $Li_{0.9\sim0.5}CoO_2$ is metallic. Thus, it is critical to monitor the electronic conductivity in real time during the charge/discharge process. However, most of the previous measurements on the electronic conductivity of LCO, so far, are limited to the bulk materials or

polycrystalline films under ex-situ conditions [10, 13], and the intriguing IMT of LCO has not been studied on different crystal facets at the nanoscale. Direct visualization of the electronic conductivity evolutions on different crystal faces enable better understanding the origin of polarization-dependent battery performance. Recently, new techniques have been developed to allow the Atomic Force Microscopy (AFM) to be operated in liquid conditions [14-17], which can image the cathode materials at charging and discharging processes [18, 19], thus providing the capability to directly probe the physical-chemical properties of the liquid/solid interface. Here we employed the *in situ* current-sensing Atomic Force Microscopy (CSAFM) to study the interfacial conductivity on the surface of LCO crystal grains and to probe the IMT on a certain crystal face. Since the extraction of Li-ions from the LCO host crystal lattice will create local Li-poor crystal region and increase the conductivity [20, 21], the nano-conductivity mapping on individual grains can further reveal the details of Li-ions migration during the deintercalation [22].

The cathode surface physicochemical properties have significant impacts on the adsorption and decomposition of electrolytes as well as the formation of electrode surface passivation layer [23, 24]. However, only few studies focused on this impact of cathode surface atom species and their arrangements. In many previous studies, the approximated electronic structure theory was introduced to explain the formation of surface passivation film [25, 26]. For the high-voltage cathode materials, the chemical potential of cathode materials might locate below the highest occupied molecular orbital (HOMO) when it is charged at > ~4.5 V vs lithium. Thus, the cathode will oxidize the electrolyte until a cathode electrolyte interphase (CEI) is formed to block the electron transfer from the electrolyte HOMO to the cathode [25, 26]. However, experimental results show that CEI layer can grow in a low charge voltage range (<4.2 V vs lithium) [27] and even can be formed as soon as the electrode is soaked in the electrolyte [28]. Recently, it is discovered that the decomposition voltage of the electrolyte on cathode is not directly equivalent to the HOMO level, but to the electrolyte oxidation potential (-$eE_{oxidation}$) [29]. This can well explain the CEI formation at lower charge voltage, but it is still lacking consideration for the adsorption effects of cathode surface on electrolyte molecular. Moreover, only few studies discussed the formation mechanism of CEI [30] and the catalysis effects of exposed metal (Co/Ni/Mn) atoms on the cathode surface.

In this study, polycrystalline LCO thin film with preferentially exposed $\{10\bar{1}1\}$ and (0003) facets were successfully deposited in a controllable manner. Their crystal structures and grain shapes were studied by electron microscopy. *In situ* XRD and CSAFM were employed to probe the Li-ion de-intercalation model and electronic conductivity on (0003) and $\{10\bar{1}1\}$ facets. The compositions and thicknesses of the surface passivation layers on each kind of electrode was studied by X-ray photoelectron spectroscopy (XPS). The adsorption and formation of the surface passivation layer was also confirmed by DFT calculations. Three key factors including the lithium diffusion, electronic conductivity, and formation of surface layers were studied in detail towards cathode electrochemical performances. The better rate and cycle performances of cells with $\{10\bar{1}1\}$ preferred orientation electrode was attributed to its straight lithium diffusion channels and better electronic conductivity compared to that with (0003). However, the lower adsorption energy of $\{10\bar{1}1\}$ facets toward the decomposition of organic molecules contributes to the adsorption and decomposition of electrolyte, which cause the formation of thick CEI and reduce the Coulombic efficiency during the initial cycle.

2. Experimental Section

2.1 Thin film preparations and characterization

Polycrystalline lithium cobalt oxide thin films with preferred orientations of (0003) and $\{10\bar{1}1\}$ were grown by using radio frequency magnetron sputtering. The deposition chamber was evacuated using a turbo-molecular pump to an initial pressure of 4×10^{-4} Pa and kept at a working pressure of 0.5 Pa. Aluminium foils (Macklin, purity 99.0%, 10 μm) were used as both substrates and current collectors. The substrate temperature was kept at 500 ℃. Deposition was conducted with a total gas flow amount of 50 sccm and the gas flow ratio of Ar : O_2 was kept at 4:1 and 1:1 for (0003) and $\{10\bar{1}1\}$ preferred orientation respectively. The sputtering was conducted at power of 100 W for 4 hours, and sample/target distance was fixed at 10 cm. The thickness of the thin films was controlled at about 500 nm.

The crystalline structure and orientation of the as-deposited LCO films were determined by X-ray diffraction (Rigaku Ultima, Cu radiation, λ=0.15406 nm). The surface morphology of thin films was captured by scanning electron microscopy (SEM, Hitachi SU-8010). TEM and STEM-HAADF

images were captured by FEI TALOS F200X. Thin film cross-sections were prepared by focused ion beam (ZEISS CROSSBEAM 550). The in situ XRD electrochemical cells were assembled in an Ar-filled glove box. Linear sweep voltammetry (LSV) of the LCO film was carried out at a voltage step of 0.02 mV s^{-1} from 3.6 to 4.2 V, and the X-ray spectra were recorded at a set time interval of 10 min. The work functions of the films were recorded using Kelvin probe force microscopy (KPFM) measurements (Bruker Dimension Icon). Surface chemistry of the disassembled first charged electrode was characterised using an X-ray Photoelectron Spectroscopy (XPS, ESCALAB 250 Xi, USA). The binding energy (B.E.) was calibrated using the C sp2 peak of aliphatic moieties at 284.8 eV. The charged electrodes were washed in dimethyl carbonate in an argon-filled glove-box and transferred into XPS chamber through sample transfer box (Thermo Fisher Inc.) to prevent exposure to the atmosphere. XPS was conducted at different sample spot to exclude CEI lateral inhomogeneous distributions. The CSAFM was performed based on Bruker Icon. As shown in the Fig. 1, the potentiostat (CHI760E, Chenghua Instrument) was used to control electrode deintercalation in the CSAFM characterization. A specially designed insulated probe with an exposed conductive apex was employed for the interfacial conductivity measurements using a tip radius of approximately 50 nm [14, 16]. A constant voltage (-50 mV) was applied between the samples and tip observing at different deintercalation states according to the *in situ* XRD results. The tip current is Non-faraday capacitance current and derives from direct conduction between the metal tip apex and the conductive local region. More experimental details about the CSAFM tests and instruments can be found in Fig. S2 in the supplementary information.
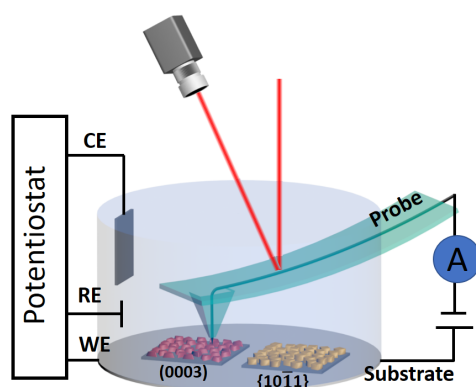

Fig. 1 The scheme and picture of *in situ* current-sensing Atomic Force Microscopy (CSAFM).

2.2 Electrochemical measurements

6

Coin half-cells were assembled in Ar-filled glovebox to measure the electrochemical properties. LCO thin film electrode acted as the cathode, Li foil as the anode and ethylcarbonate (EC) and dimethyl carbonate (DMC) (1: 1 vol %) solution with an addition of 1M LiPF6 as the liquid electrolyte. LCO thin-film electrodes were punched as a disc with R=0.6 mm. All electrochemical performances were measured at 27 °C. Galvanostatic charge-discharge was carried out at 0.2 C between 3.0 and 4.2 V. Rate performance measurements were conducted at the charge/discharge rate of 0.3, 0.6, 1.2, 2.4 and 4.8 C.

2.3 DFT Calculation

Calculations in this work were carried out using the Vienna ab initio simulation package (VASP) [31-32] with the projector augmented wave (PAW) method [34]. Exchange-correlation interactions were treated with generalized gradient approximation (GGA) [35] in the Perdew-Burke-Ernzerhof (PBE) form [36]. The on-site electron-electron interactions were taken into account by performing GGA+U level calculations for Co-3d electrons. The value of the effective U was set to 4.91 eV, as suggested in the previous work [37]. Spin polarized calculations were performed, and the plane-wave basis set for the kinetic energy cutoff was 500 eV. The Brillouin zone was sampled using Monkhorst–Pack scheme with 4×4×1 k-point grid. Atomic positions were optimized by using the quasi-Newton method until the forces were less than 0.05 eV/Å. The adsorption energy (E_{ads}) for the adsorbate is defined as [23, 38]:

$$E_{ads} = E_{adsorbate-surface} - E_{surface} - E_{adsorbate}$$

Where $E_{adsorbate-surface}$, $E_{surface}$ and $E_{adsorbate}$ are the energies of the surface with adsorbate adsorption, clean surface and gas-phase adsorbate, respectively.
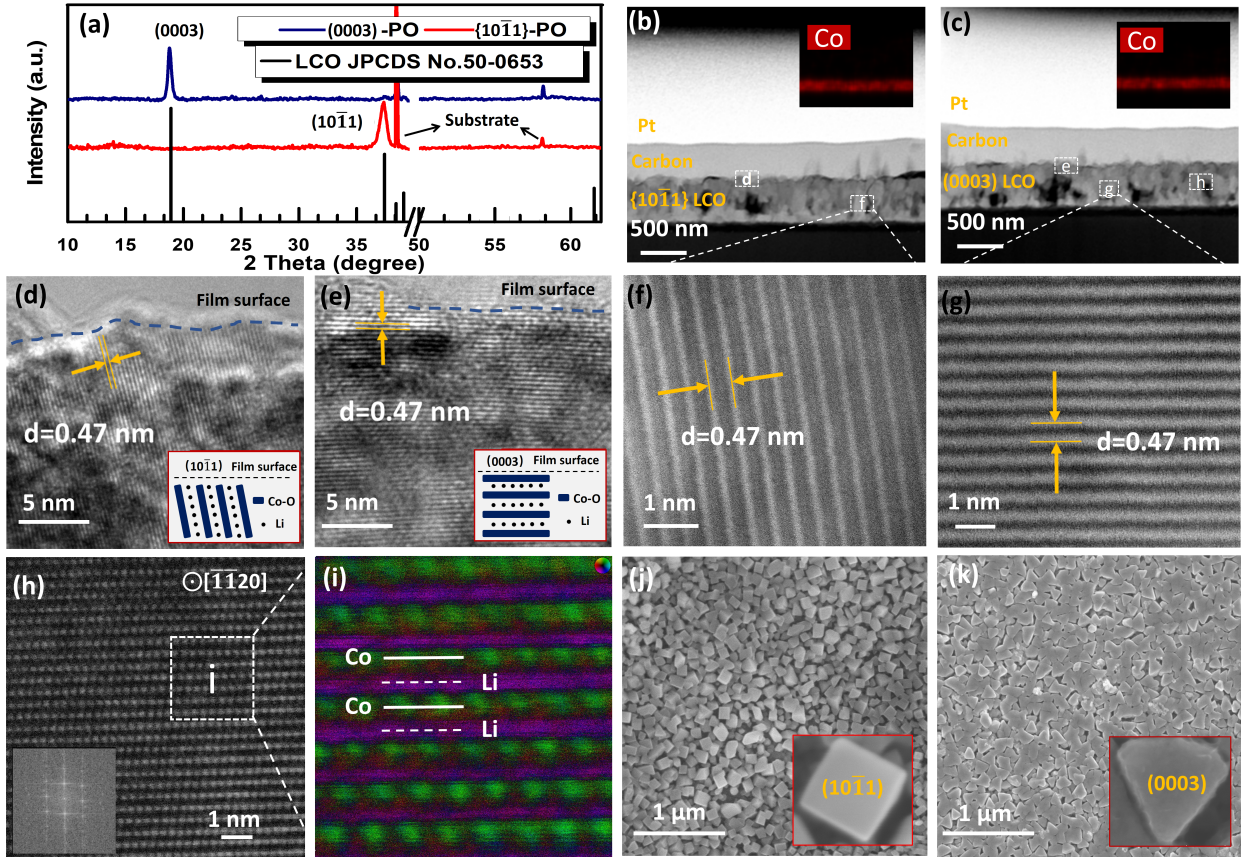
3. Results and discussion

Fig. 2 Structure characterizations of {10$\bar{1}$1} preferred orientation ({10$\bar{1}$1}-PO) and (0003) preferred orientation ((0003)-PO) thin films. (a) XRD patterns. (b) and (c) HAADF-STEM images and Co EDS mapping (inset) of cross-sectional thin-film. (d) and (e) TEM image of the cross-sectional film surface area on Fig. 1 (b) and (c), respectively. (f) and (g) HAADF-STEM images of the middle region of the film in Fig. 1 (b) and (c), respectively. (h) HAADF-STEM image of Co atomic columns along the [$\bar{1}\bar{1}$20] zone-axis. (i) The Differential Phase Contrast (DPC)-STEM image at high magnification. (j) and (k) SEM images of {10$\bar{1}$1}-PO and (0003)-PO thin films surface, the insets are two typical crystal grain shapes.

Fig. 2a shows the XRD patterns of as-prepared LCO thin films with two preferred orientations ({10$\bar{1}$1} and (0003)). Only one diffraction peak can be observed in each thin film sample. These two diffraction peaks (at 2θ ≈ 18.9° and 37.3°) are attributed to (0003) and (10$\bar{1}$1) crystal planes of R$\bar{3}$m LiCoO$_2$, respectively. Here the (0003) and {10$\bar{1}$1} preferred orientations are denoted as (0003)-PO and {10$\bar{1}$1}-PO, respectively. Figs. 2b and c show STEM cross-sectional views of the two types of sample as-prepared by FIB. The thicknesses of both thin films are measured to be about 500 nm. Different preferred orientations of LCO thin films result in exposing different crystal planes to the electrolyte. As

8

seen in the near-surface area of the cross-sectional high resolution TEM images (Figs. 2d and e), the lattice fringes with $d_{(0003)}$=0.47 nm prove the structure models in the inset. For $\{10\bar{1}1\}$-PO, the fast Li$^+$ diffusion planes intersect with the film surface. However, for the (0003)-PO, the lithium diffusion channels are parallel to the film surface. The TEM image Figs. 2f and g show that the diffusion channels between Co-O layers are also observed in the middle region of the film, which indicates the as-prepared thin film electrodes have preferred orientation throughout their thickness. The atomic resolution HAADF-STEM image along the $[\bar{1}\bar{1}20]$ direction in Fig. 2h was captured by rotating the (0003)-PO sample. The clearly observed Co atomic columns confirm that the as-prepared LCO thin film is highly crystalline with R$\bar{3}$m structure [39]. In Fig. 2i, the Differential Phase Contrast STEM image shows a uniform electronic/magnetic deflection angle around each cobalt atom, which indicates that the cobalt atoms in the as-deposited thin film are dominated by the stoichiometric non-magnetic Co^{3+}. Figs. 2j and k are typical SEM images of the film surfaces exhibiting crystal grains with characteristically symmetric facets. The morphology of the $\{10\bar{1}1\}$-PO thin film in Fig. 2j consists of many 4-mm symmetry crystal grains with cuboidal appearance. By contrast, the (0003)-PO thin film in Fig. 2k shows many triangular domains with 3-mm symmetry. These two kinds of grains are consistent with previous reports, which suggest that grain appearances correlate to the orientations and symmetries of the R$\bar{3}$m LCO crystal [6, 40]. To sum up the structure data, highly crystallization and stoichiometric LCO (0003)-PO and $\{10\bar{1}1\}$-PO thin films with distinct symmetric facets were successfully prepared.
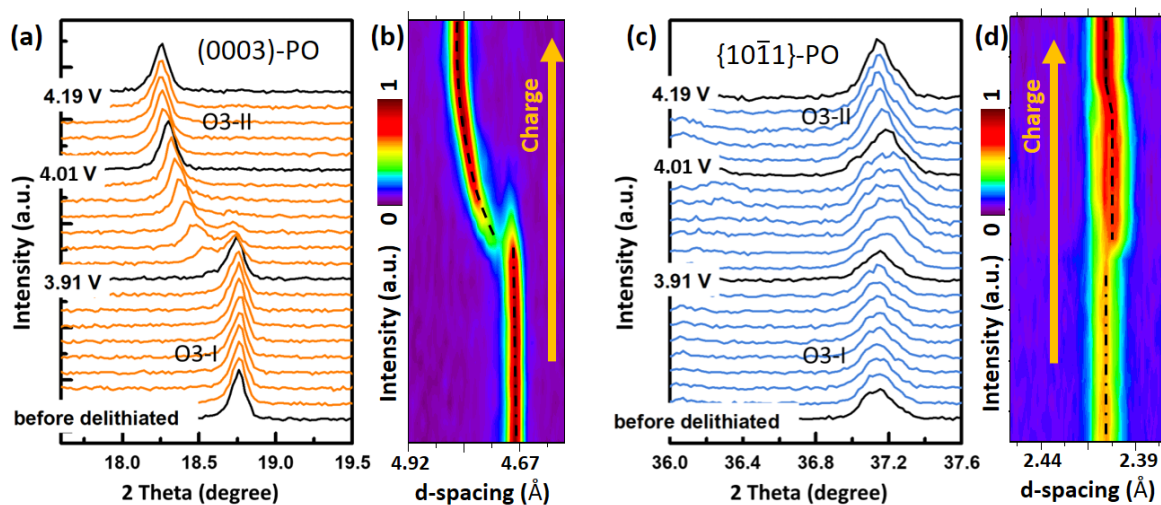

Fig. 3 (a)/(b) and (c)/(d) The *in situ* 2D XRD/Contour Spectrum of (0003)-PO and $\{10\bar{1}1\}$-PO electrode plotted in the regions with Bragg reflections during the 1st de-intercalation respectively.

In situ XRD spectra were conducted at different electrode potentials by Linear Sweep Voltammetry (LSV) scan (supplementary information Fig. S1) for both (0003) and $\{10\bar{1}1\}$ thin film electrodes. Fig. 3 shows the *in situ* XRD patterns regarding the Bragg reflections of (0003)-PO and $\{10\bar{1}1\}$-PO LCO thin films respectively during the 1st de-intercalation. As shown in Fig. 3a, (0003) diffraction peak of O3-I phase remains constant with the voltage sweeping up till 3.91 V, and then a new peak belonging to the O3-II phase emerges at around 3.91 V corresponding to the beginning of the O3-I→O3-II phase transition (IMT). As shown in Fig. 3b, in the charge process, the peak intensity of the O3-I phase decreases as increasing amount of O3-II phase is formed, and the d-spacing of O3-II phase increases from about 4.78 to 4.85 Å. As for the diffraction spectra of $\{10\bar{1}1\}$-PO thin films shown in Fig. 2c, a new peak, corresponding to the $(10\bar{1}1)$ diffraction peak of O3-II phase, grows on the high-angle side of existing $(10\bar{1}1)$ peak during the 3.91-4.01 V. Then, the peak of O3-II phase comes back to the position of original $(10\bar{1}1)$ peak with stronger diffraction intensity (as shown in Fig. 3d) between the voltage range of 4.01-4.19 V. The $(10\bar{1}1)$ peak position for the O3-II phase is close to the O3-I phase because the lattice parameters "a" and "b" of O3-I/II phase are very similar [41]. The phase transition results during the first de-intercalation are in accord with previous reports [42, 43].

Based on the *in situ* XRD and LSV analysis, four de-intercalation states for CSAFM characterization were chosen with: before de-intercalation state, charge voltage V_c=3.91 V, 4.01 V and 4.19 V states. They are corresponding to four typical phase transition states of LCO. Figs. 4a and b are the results of *in situ* CSAFM characterizations (a larger scanning area can be found in supplementary information Fig. S3). During CSAFM measurements, a constant voltage was applied between tip and sample. The higher Tip-Sample contact (TSC) current in the local region is, the higher the conductivity is, which also means the lower lithium concentration it has.
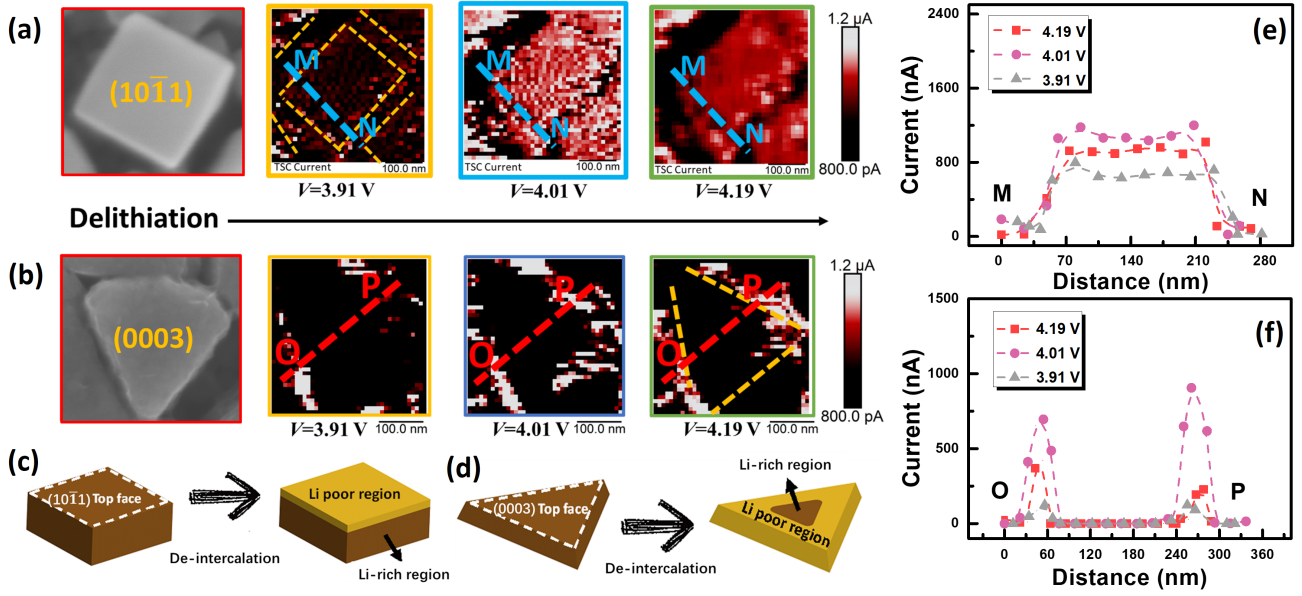
Fig. 4 (a) and (b) The tip-sample contact current (TSC) signal on the surface of $\{10\bar{1}1\}$-PO and (0003)-PO electrode at Vc=4.19 V, 4.01 V, 3.91 V, during the 1st de-intercalation, respectively. (The first picture on the left for each figure is SEM image) (c) and (d) The diagram of lithium concentration distributions in the both grains. (e) and (f) The TSC current as a function of the distance from M to N in Fig. 4 (a) and from O to P in Fig. 4 (b).

As shown in Fig. S3, before de-intercalation, the captured TSC currents on the (0003) and $\{10\bar{1}1\}$-PO electrodes keep at the noise level due to their insulative initial state. Fig. 4a is the distribution of TSC current on a single grain $(10\bar{1}1)$ surface during the first de-intercalation. When the electrode is charged at 3.91 V (corresponding to the onset phase transition voltage as shown in Fig. 3c), the average TSC current increases to 500~700 nA on the $(10\bar{1}1)$ facet, which can be attributed to the de-intercalation of Li-ion from the topmost crystal grain. In another word, the TCS current was enhanced by the de-intercalation of Li-ion resulted in the IMT (conductivity change) on the top region of the grains. When the electrode voltage was enhanced to 4.01 V, the average TSC current on the $\{10\bar{1}1\}$ facet was increased to 1100~1200 nA, which indicates that the initial O3-I phase with low conductivity is gradually changed as the O3-II phase with a higher conductivity. However, when the electrode voltage was enhanced to 4.19 V, the average TSC current was slightly decreased to about 950 nA. This is attributed to continuously growth of the insulative CEI during the charge processes [27, 29, 44]. Fig. 4b shows the distribution of TSC current on (0003) crystal face for 3 de-intercalation states. At the beginning of the charging, the (0003) face shows a better conductivity on the grain boundary region,

which indicates that the IMT is formed primarily on the grain boundaries instead of the inner region. During the whole de-intercalation at each voltage, the conductivity difference between the (0003) inner facets and boundary regions can be distinguished. The slight decrease of TSC current on the boundary regions should also be attributed to the accumulation of surface passivation layers as discussed in the Fig. S4. Based on the these TSC current maps, the lithium concentration distribution in both (0003) and {10$\bar{1}$1}-PO grains are depicted in Fig. 4c and d. The models show that the Li-poor regions with high electronic conductivity are the area detected by the higher TSC current. Figs. 4d and e show the TSC current as a function of the distance along M-N and O-P lines in Figs 4a and b, respectively. The "n" and "u" shape TSC current curves can be observed for the (10$\bar{1}$1) and (0003) LCO crystal grains, which can be explained by the "Li-rich core" de-intercalation mechanism.

Figs. 5a and b show two possible Li-ion de-intercalation processes which result in "Li-rich core" and "Li-poor core" regions in the LCO grain respectively. These processes occur when LCO cathode is delithiated. For the mechanism resulting in a "Li-rich core", the first layer of Li-ions exposed to the outside are driven to migrate outwards. Once the first layer is removed, the next inner layer of Li-ions will also follow the same procedure and so forth. This results in the LCO grain to form Li-poor states around the surface region and Li-rich state at the core. In contrast, Fig. 5b displays "Li-poor core" regions due to a different type of lithium de-intercalation mechanism. Instead of the lithium layers migrating outwards each time, once the outmost layer is vacant, all other inner layers will move towards the surface, leaving behind an empty layer at the core. This keeps repeating until the core is in a Li-poor state and the surface is surrounded in Li-ions.

Based on the "n" and "u" shapes observed from the TSC current curves for both LCO grains of (0003) and {10$\bar{1}$1}, it can be concluded that the LCO grain resulting in "Li-rich core" from de-intercalation mechanism is well suited to LCO crystal grain. For the {10$\bar{1}$1} crystal grain, its Li-ion diffusion channel is about 78 degrees from the film surface, as shown in Fig. 5c, "Li-rich core" de-intercalation mechanism makes the regions near the surface to keep at Li-poor states (high conductivity) during de-intercalation. This therefore explains why a high TSC current in the whole grain surface as shown in Fig. 4a. Similarly, for the (0003) grain in Fig. 5d, its Li-ion diffusion channel is parallel to film surface. "Li-rich core" de-intercalation mechanism makes the outer regions Li-poor and inner

regions Li-rich states. This observation is noticed during TSC current experiment, as high current is observed in outer region and low current in the inner regions as displayed in Fig. 4c.
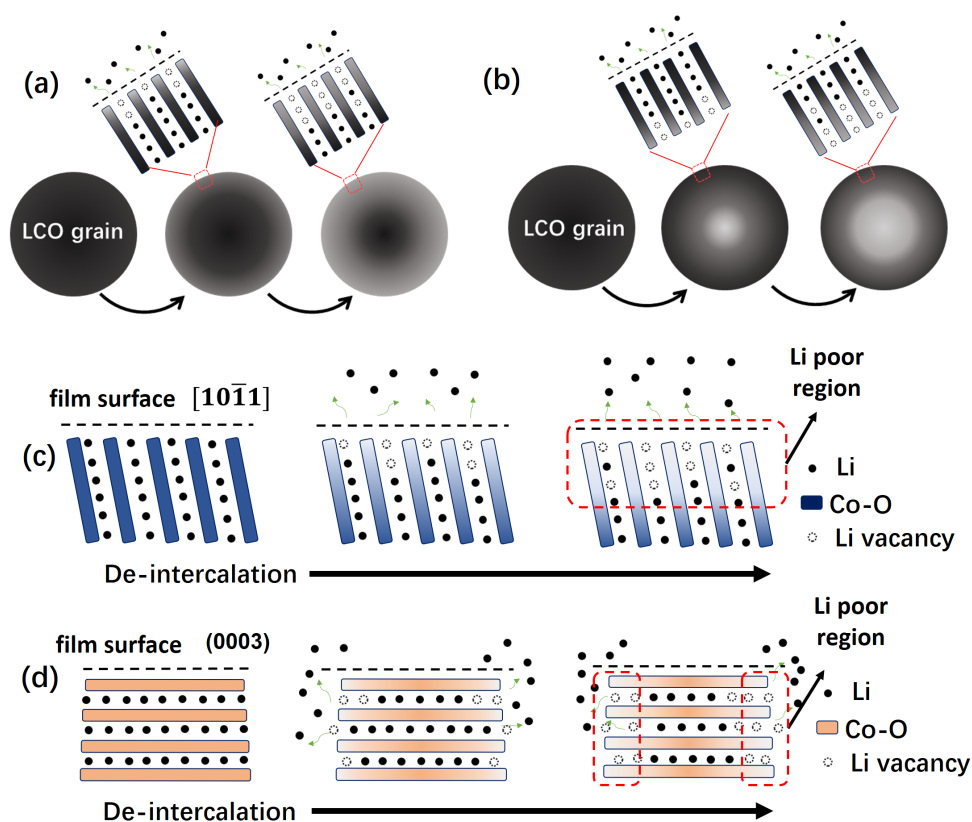

Fig. 5 (a) and (b) are the "Li-rich core" and "Li-poor core" model. The schematic illustrating the movement of Li ions during de-intercalation in an LCO crystal grain. The darker regions display Li-rich areas and lighter regions show Li-poor areas. (c) and (d) The cross-section schematic of Li-ions de-intercalation mechanism for $(10\bar{1}1)$ and (0003) single grain, respectively.

Fig. 6a is the cycle performances of the (0003) and $\{10\bar{1}1\}$-PO half-cells. From the figure, it can be seen that the initial charge capacity of the cell with $\{10\bar{1}1\}$-PO cathode exceeds 140 mAh/g, and after 70th charge and discharge cycles, it is still kept at around 110 mAh/g. The charge capacities of the cell with (0003)-PO cathode are around 121 mAh/g and 92 mAh/g at the 1st and 70th cycles, respectively. By comparison, it is found that the cell with $\{10\bar{1}1\}$-PO cathode has 20% higher cycle capacity than that with (0003)-PO cathode. The sparse TSC current on the (0003) crystal grain surface in Fig. 4c, indicating the less conductive surface area, implies that the worse cycle capacity of the (0003)-PO electrode may not only attribute to its sluggish lithium diffusion dynamics, but also to the poor electronic conductivity of cathode film. The charge plateau is observed at around 3.92 V for the $\{10\bar{1}1\}$-

PO cell and at 3.98 V for the (0003)-PO cell in Fig. 6b. This difference should derive from the serious polarization of (0003)-PO electrodes, which results in the increase of inner resistivity of cell. An overshooting voltage caused by the electrode polarization can be observed on the 1st charge curve of the (0003)-PO cell which is consistent with the previous reports [43-45]. Furthermore, as shown in Fig. 6c, the lower discharge voltage plateau of (0003)-PO cell observed on the discharge curves, also confirms its serious electrode polarization of the (0003)-PO cell. Consequently, the {10$\bar{1}$1}-PO cell shows a much better rate performance than (0003)-PO cell, as seen in Fig. 6d.
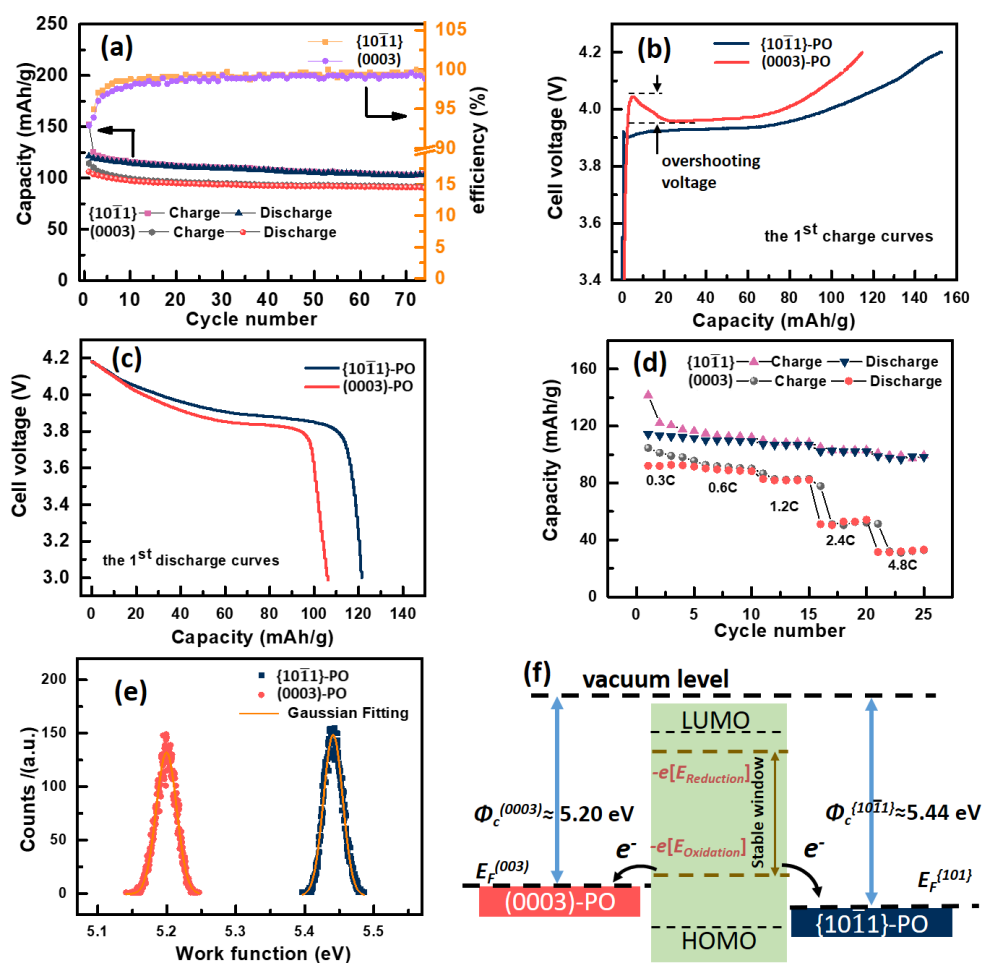

Fig. 6 (a) Galvanostatic cycling performances; (b) and (c) Charge and discharge voltage curves; (d) Rate performances of (0003)-PO and {10$\bar{1}$1}-PO cells. (e) The surface work function of (0003)-PO and {10$\bar{1}$1}-PO electrodes measured by KPFM. (f) Schematic energy diagram of the LCO/electrolyte interface. Φ_c is the work functions of a cathode. LUMO and HOMO are the lowest unoccupied molecular orbital and the highest occupied molecular orbital, respectively. $E_{Reduction}$ and $E_{Oxidation}$ are the reduction and oxidation potentials of the electrolyte, respectively.

Another difference in the electrochemical performance of the (0003) and $\{10\bar{1}1\}$-PO electrode is the initial Coulombic efficiency. The $\{10\bar{1}1\}$-PO cell shows unexpected lower initial Coulombic efficiency (80 %) compared to (0003)-PO cell (92 %). The lower Coulombic efficiency should normally attribute to the formation of thicker CEI induced by the irreversible electrolyte decomposition. However, in LCO composite-electrode, the CEI formation is not commonly observed within 3-4.2 V charge voltage range. Presumably, the CEI formation on LCO thin film cathode, especially the cathode with $\{10\bar{1}1\}$ faces, should be activated by the preferred exposed facets with different atom arrangements and surface electronic structure. The KPFM and X-ray photoelectronic spectroscopy (XPS) characterizations were employed to study the CEI on the electrode surfaces.

From the thermodynamic point of view, it is supposed that when the chemical potential (Fermi energy E_F) of LCO is below the electrolyte oxidation potential ($-eE_{oxidation}$), LCO will oxidize the electrolyte with the formation of a passivation layer (CEI) on the cathode surface [29]. Fig. 6e shows the surface work functions (Φ_c) of the $\{10\bar{1}1\}$-PO and (0003)-PO thin films before de-intercalation measured by the KPFM. The KPFM images and its detail calculation from contact potential difference (CPD) can be found in supplementary information(shown in Fig. S5). The Φ_c values of $\{10\bar{1}1\}$-PO and (0003)-PO thin films are found to be about 5.44 eV and 5.20 eV, respectively. A larger work function value means a lower E_F. Therefore, as shown in the energy diagram in Fig. 6f, compared with the (0003)-PO electrode, the lower E_F of $\{10\bar{1}1\}$ crystal faces have stronger thermodynamic driving force to grab the electrode from the electrolyte [47]. This means that the direct oxidation of the electrolyte on the electrode/electrolyte interface is more likely to occur on the $\{10\bar{1}1\}$ faces. Hence, a thicker CEI film may be formed on the $\{10\bar{1}1\}$-PO electrode surface.
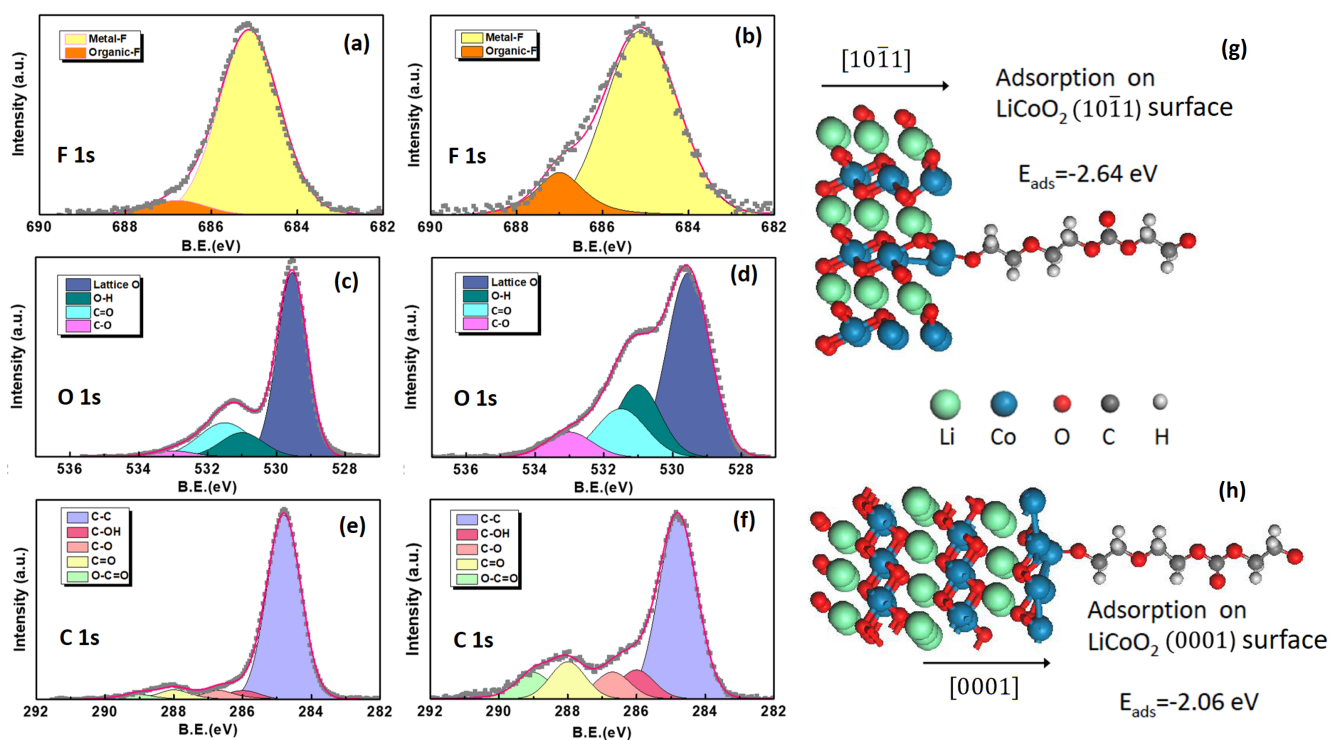
Fig. 7 (a, b) F1s, (c, d) O1s and (e, f) C1s XPS of (0003)-PO and {10$\bar{1}$1}-PO thin film electrode after the first charge. The assignments of all peaks are summarized in Table S1 in the supplementary information. (g) and (h) The model and adsorption energy of a chain molecule on {10$\bar{1}$1} and (0003) faces.

Figs. 7 (a-f) show the XPS results of the (0003)-PO and {10$\bar{1}$1}-PO thin film electrodes after the first charge. As shown in Figs. 7a and b, the observed two F1s peaks at 685 eV and 687 eV are attributed to the metal-F (LiF) and organic-F, respectively [48]. The fluorine arises from the degradation of ethylcarbonate (EC) activated by interactions with PF_5 and LCO cathode surfaces [49]. The higher peak area ratio of organic-F/metal-F in {10$\bar{1}$1}-PO electrode indicates more organic species ($C_XH_YO_Z$) in its CEI. The O 1s spectra of as-prepared and soaked LCO thin film surface are provided in Fig. S6 (a). By comparison, as shown in the O 1s spectra in Figs. 7c and d, the three peaks of organic decomposition, including organic species (O-H, C-O and C=O), were detected after the first charge. Additionally, a higher intensity ratio of organic species in {10$\bar{1}$1}-PO CEI can be found, which indicates that a stronger decomposition signal was formed in the cycled {10$\bar{1}$1}-PO electrode surface than that in the (0003)-PO electrode. The different CEI thicknesses are evaluated by using the spectral weight of the lattice oxygen peak and the CEI related oxygen peaks according to the equation (1) in supplementary information. The estimated thicknesses are about 4.5 Å and 11.4 Å for the (0003) and {10$\bar{1}$1}-PO, respectively. In the

C1s spectra in Figs. 7e and f, the charged {10$\bar{1}$1}-PO electrode shows a higher overall intensity of C1s peaks (C-OH, C–O, C=O, and O-C=O) than the (0003)-PO electrode. This further confirms the existence of organic decomposition on the charged electrode surface [50]. Moreover, the thicker electrolyte decomposition covered on the {10$\bar{1}$1}-PO thin-film electrode surface will reduce the peak intensities of the Co and Li, as seen in Fig. S6 (b). In conclusion, the XPS characterizations indicate that: after the first charge, the CEI, also known as an electrolyte decomposition consisted of LiF and organic compounds ($C_XH_YO_Z$), is formed on the electrode surface, and more organic species can be found in the CEI layer of {10$\bar{1}$1}-PO electrode than that on the (0003)-PO one.

The organic species in CEI detected by XPS should derive from the C-H bond scission in dimethyl carbonate (DMC) [24] and/or the ring open of EC [50] on the LCO surface. Then the decomposed solvent molecules undergo a series of chain reactions and convert to polymers/oligomers molecules which adsorbed at the electrode outmost-surface metal atoms and form the CEI [23, 30]. Therefore, the thickness and ingredients of the CEI layers are dominated by the electrode outmost-surface atomic structure. To confirm the experimental observations, we constructed a simple CEI model consisted of a model chain molecule [23] adsorbed on the $LiCoO_2$ (10$\bar{1}$1) and (0001) surface slabs. The stability of the interfaces was evaluated from the calculated adsorption energies using first-principles calculations. As shown in Figs. 7g and h, the calculated adsorption energies are both negative for both $LiCoO_2$ (10$\bar{1}$1) and $LiCoO_2$ (0001) surfaces, indicating that the adsorption process is thermodynamically favorable at Co sites for both crystal surfaces. In addition, the adsorption energy of the model chain molecule on the (10$\bar{1}$1) surface is -2.64 eV, about 0.58 eV lower than that on the (0001) surface. The results indicate that the polymer/oligomer molecular adsorption and charge transfer are more likely to occur on {10$\bar{1}$1}-PO electrodes with more negative adsorption energy. Therefore, the calculations unambiguously support that the electrolyte decomposition is more easily to be adsorbed and accumulated on the {10$\bar{1}$1} crystal facets than that on the (0003) crystal facets.

4. Conclusions

In conclusion, the Li-ions migration was traced on a single crystal grain from both (0003) and {10$\bar{1}$1} crystal facets by *in situ* CSAFM and two different electronic conductivity evolutions were

discovered and discussed based on the "lithium-rich core" model. During the *in situ* CSAFM tests, the TSC current on the boundary region of (0003) facet was increased to 10^3 times stronger than that on the inner region. While on the whole $(10\bar{1}1)$ facet, it was increasing uniformly. As a result, the $\{10\bar{1}1\}$-PO thin film electrode has more conductive surface areas and shows smaller electrode polarization than (0003)-PO thin film electrode. This is beneficial for reducing the internal resistance of the battery. Moreover, an unexcepted lower initial Coulombic efficiency was found in the first cycle of $\{10\bar{1}1\}$-PO electrode, which is caused by the formation of a thicker CEI film with higher percentage of organic ingredients. The formation mechanism was interpreted as the larger surface work function value and more negative adsorption energy of electrolyte decomposition on the $\{10\bar{1}1\}$ crystal facets. At last, this work suggests that the metal adsorption active sides on cathode surface may contribute to the adsorption and decomposition of electrolyte solvent molecules, which may reduce the decomposition voltage of electrolyte. Therefore, it is essential to carefully optimize the exposed crystal facets of high-voltage cathode materials not only to promote the diffusion of lithium-ions, but also to enhance the cathode surface stability.

Conflicts of interest

There are no conflicts to declare.

Author Contributions

⊥ Y. Chen and Y. Niu. contributed equally.

Acknowledgements

References

[1] J. Qian, L. Liu, J. Yang, S. Li, X. Wang, H.L. Zhuang, Y. Lu, Electrochemical surface passivation of $LiCoO_2$ particles at ultrahigh voltage and its applications in lithium-based batteries, Nat Commun. 9 (2018) 4918.

[2] M. Yoon, Y. Dong, Y. Yoo, S. Myeong, J. Hwang, J. Kim, S.H. Choi, J. Sung, S.J. Kang, J. Li, J. Cho, Unveiling Nickel Chemistry in Stabilizing High-Voltage Cobalt-Rich Cathodes for Lithium-Ion Batteries, Advanced Functional Materials. 30 (2019) 1907903.

[3] S. Kuppan, A.K. Shukla, D. Membreno, D. Nordlund, G. Chen, Revealing Anisotropic Spinel Formation on Pristine Li- and Mn-Rich Layered Oxide Surface and Its Impact on Cathode Performance, Advanced Energy Materials. 7 (2017) 1602010.

[4] C. Dellen, H.G. Gehrke, S. Möller, C.L. Tsai, U. Breuer, S. Uhlenbruck, O. Guillon, M. Finsterbusch, M. Bram, Time-of-flight secondary ion mass spectrometry study of lithium intercalation process in $LiCoO_2$ thin film, Journal of Power Sources. 321 (2016) 241-247.

[5] Z. Yang, P.V. Ong, Y. He, L. Wang, M.E. Bowden, W. Xu, T.C. Droubay, C. Wang, P.V. Sushko, Y. Du, Direct Visualization of Li Dendrite Effect on $LiCoO_2$ Cathode by In Situ TEM, Small. 14 (2018) e1803108.

[6] S. Takeuchi, H. Tan, K.K. Bharathi, G.R. Stafford, J. Shin, S. Yasui, I. Takeuchi, L.A. Bendersky, Epitaxial $LiCoO_2$ Films as a Model System for Fundamental Electrochemical Studies of Positive Electrodes, Acs Appl Mater Interfaces. 7 (2015) 7901-7911.

[7] Y. Yoon, C. Park, J. Kim, D. Shin, Lattice orientation control of lithium cobalt oxide cathode film for all-solid-state thin film batteries, Journal of Power Sources. 226 (2013) 186-190.

[8] J.B. Goodenough, How we made the Li-ion rechargeable battery, Nature Electronics. 1 (2018) 204-204.

[9] J. Alper, The Battery: Not Yet a Terminal Case, Science. 296 (2002) 1224-1226.

[10] T. Motohashi, Y. Sugimoto, Y. Masubuchi, T. Sasagawa, W. Koshibae, T. Tohyama, H. Yamauchi, S. Kikkawa, Impact of lithium composition on the thermoelectric properties of the layered cobalt oxide system LixCoO$_2$, Physical Review B. 83 (2011).

[11] C.A. Marianetti, G. Kotliar, G. Ceder, A first-order Mott transition in LixCoO$_2$, Nat Mater. 3 (2004) 627-631.

[12] M. Ménétrier, I. Saadoune, S. Levasseur, C. Delmas, The insulator-metal transition upon lithium deintercalation from LiCoO$_2$: electronic properties and 7Li NMR study, Journal of Materials Chemistry. 9 (1999) 1135-1140.

[13] M. Nishizawa, S. Yamamura, Irreversible conductivity change of Li$_{1-x}$CoO$_2$ on electrochemical lithium insertion/extraction, desirable for battery applications, Chemical Communications. 16 (1998) 1631-1632.

[14] M.R. Nellist, Y. Chen, A. Mark, S. Godrich, C. Stelling, J. Jiang, R. Poddar, C. Li, R. Kumar, G. Papastavrou, M. Retsch, B.S. Brunschwig, Z. Huang, C. Xiang, S.W. Boettcher, Atomic force microscopy with nanoelectrode tips for high resolution electrochemical, nanoadhesion and nanoelectrical imaging, Nanotechnology. 28 (2017) 095711.

[15] M.R. Nellist, F.A.L. Laskowski, J. Qiu, H. Hajibabaei, K. Sivula, T.W. Hamann, S.W. Boettcher, Potential-sensing electrochemical atomic force microscopy for in operando analysis of water-splitting catalysts and interfaces, Nature Energy. 3 (2017) 46-52.

[16] J. Jiang, Z. Huang, C. Xiang, R. Poddar, H.J. Lewerenz, K.M. Papadantonakis, N. Lewis, B. Brunschwig, Nanoelectrical and Nanoelectrochemical Imaging of Pt/p-Si and Pt/p$^+$-Si Electrodes, Chemsuschem. 10 (2017) 4657-4663.

[17] I.V. Pobelov, M. Mohos, K. Yoshida, V. Kolivoska, A. Avdic, A. Lugstein, E. Bertagnolli, K. Leonhardt, G. Denuault, B. Gollas, Electrochemical current-sensing atomic force microscopy in conductive solutions, Nanotechnology. 24 (2013) 115501.

[18] R.R. Liu, X. Deng, X.R. Liu, H.J. Yan, A.M. Cao, D. Wang, Facet dependent SEI formation on the LiNi$_{0.5}$Mn$_{1.5}$O$_4$ cathode identified by in situ single particle atomic force microscopy, Chemical Communications. 50 (2014) 15756-15759.

[19] Z.F. Bi, J.X. Wu, S. Yang, L. Li, P.F. Yang, Y, Shang, G.G. Shang, In situ probing behaviors of single LiNiO$_2$ nanoparticles by merging CAFM and AM–FM techniques, Nanoscale. 10 (2018) 2916-2922.

[20] X. Zhu, C.S. Ong, X. Xu, B. Hu, J. Shang, H. Yang, S. Katlakunta, Y. Liu, X. Chen, L. Pan, J. Ding, R.W. Li, Direct observation of lithium-ion transport under an electrical field in LixCoO$_2$ nanograins, Sci Rep. 3 (2013) 1084.

[21] A. Moradpour, O. Schneegans, S. Franger, A. Revcolevschi, R. Salot, P. Auban-Senzier, C. Pasquier, E. Svoukis, J. Giapintzakis, O. Dragos, V.C. Ciomaga, P. Chretien, Resistive switching phenomena in Li$_{(x)}$CoO$_{(2)}$ thin films, Adv Mater. 23 (2011) 4141-4145.

[22] Y. Chen, Q. Yu, G. Xu, G. Zhao, J. Li, Z. Hong, Y. Lin, C.-L. Dong, Z. Huang, In Situ Observation of the Insulator-To-Metal Transition and Nonequilibrium Phase Transition for Li1–xCoO2 Films with Preferred (003) Orientation Nanorods, Acs Applied Materials & Interfaces. 11 (2019) 33043-33053.

[23] D. Chen, M.A. Mahmoud, J.H. Wang, G.H. Waller, B. Zhao, C. Qu, M.A. El-Sayed, M. Liu, Operando Investigation into Dynamic Evolution of Cathode-Electrolyte Interfaces in a Li-Ion Battery, Nano Lett. 19 (2019) 2037-2043.

[24] E.G. Leggesse, R.T. Lin, T.-F. Teng, C.-L. Chen, J.-C. Jiang, Oxidative Decomposition of Propylene Carbonate in Lithium Ion Batteries: A DFT Study, The Journal of Physical Chemistry A. 117 (2013) 7959-7969.

[25] J.B. Goodenough, Y. Kim, Challenges for Rechargeable Li Batteries †, Chemistry of Materials. 22 (2010) 587-603.

[26] J.B. Goodenough, K.-S. Park, The Li-Ion Rechargeable Battery: A Perspective, J Am Chem Soc. 135 (2013) 1167-1176.

[27] T. Minato, H. Kawaura, M. Hirayama, S. Taminato, K. Suzuki, N.L. Yamada, H. Sugaya, K. Yamamoto, K. Nakanishi, Y. Orikasa, H. Tanida, R. Kanno, H. Arai, Y. Uchimoto, Z. Ogumi, Dynamic Behavior at the Interface between Lithium Cobalt Oxide and an Organic Electrolyte Monitored by Neutron Reflectivity Measurements, The Journal of Physical Chemistry C. 120 (2016) 20082-20088.

[28] D. Takamatsu, Y. Koyama, Y. Orikasa, S. Mori, T. Nakatsutsumi, T. Hirano, H. Tanida, H. Arai, Y. Uchimoto, Z. Ogumi, First In Situ Observation of the LiCoO$_2$ Electrode/Electrolyte Interface by Total-Reflection X-ray Absorption Spectroscopy, Angewandte Chemie International Edition. 51 (2012) 11597-11601.

[29] P. Peljo, H.H. Girault, Electrochemical potential window of battery electrolytes: the HOMO–LUMO misconception, Energy & Environmental Science. 11 (2018) 2306-2309.

[30] Y. Zhang, Y. Katayama, R. Tatara, L. Giordano, Y. Yu, D. Fraggedakis, J.G. Sun, F. Maglia, R. Jung, M.Z. Bazant, Y. Shao-Horn, Revealing electrolyte oxidation via carbonate dehydrogenation on Ni-based oxides in Li-ion batteries by in situ Fourier transform infrared spectroscopy, Energy & Environmental Science. 13 (2020) 183-199.

[31] G. Kresse, J. Furthmüller, Efficiency of ab-initio total energy calculations for metals and semiconductors using a plane-wave basis set, Computational Materials Science. 6 (1996) 15-50.

[32] K. Zhong, R. Hu, G. Xu, Y. Yang, J.-M. Zhang, Z. Huang, Adsorption and ultrafast diffusion of lithium in bilayer graphene: Ab initio and kinetic Monte Carlo simulation study, Physical Review B. 99 (2019) 155403.

[33] R. Hu, G. Xu, Y. Yang, J.-M. Zhang, K. Zhong, Z. Huang, Effect of stacking structure on lithium adsorption and diffusion in bilayer black phosphorene, Physical Review B. 100 (2019) 085422.

[34] G. Kresse, J. Furthmüller, Efficient iterative schemes for ab initio total-energy calculations using a plane-wave basis set, Physical Review B. 54 (1996) 11169-11186.

[35] J.P. Perdew, J.A. Chevary, S.H. Vosko, K.A. Jackson, M.R. Pederson, D.J. Singh, C. Fiolhais, Atoms, molecules, solids, and surfaces: Applications of the generalized gradient approximation for exchange and correlation, Physical Review B. 46 (1992) 6671-6687.

[36] J.P. Perdew, K. Burke, M. Ernzerhof, Generalized Gradient Approximation Made Simple, Phys Rev Lett. 77 (1996) 3865-3868.

[37] F. Zhou, M. Cococcioni, C.A. Marianetti, D. Morgan, G. Ceder, First-principles prediction of redox potentials in transition-metal compounds with mathrm {LDA}+U, Physical Review B. 70 (2004) 235121.

[38] L. Huai, Z. Chen, J. Li, Degradation Mechanism of Dimethyl Carbonate (DMC) Dissociation on the $LiCoO_2$ Cathode Surface: A First-Principles Study, Acs Appl Mater Interfaces. 9 (2017) 36377-36384.

[39] H. Moriwake, A. Kuwabara, C.A.J. Fisher, R. Huang, T. Hitosugi, Y.H. Ikuhara, H. Oki, Y. Ikuhara, First-Principles Calculations of Lithium-Ion Migration at a Coherent Grain Boundary in a Cathode Material, $LiCoO_2$, Advanced Materials. 25 (2013) 618-622.

[40] Z. Li, S. Yasui, S. Takeuchi, A. Creuziger, S. Maruyama, A.A. Herzing, I. Takeuchi, L.A. Bendersky, Structural study of epitaxial $LiCoO_2$ films grown by pulsed laser deposition on single crystal $SrTiO_3$ substrates, Thin Solid Films. 612 (2016) 472-482.

[41] J.N. Reimers, J.R. Dahn, Electrochemical and In Situ X-Ray Diffraction Studies of Lithium

Intercalation in Li_xCoO_2, Journal of The Electrochemical Society. 139 (1992) 2091-2097.

[42] L. Liu, L. Chen, X. Huang, X.Q. Yang, W.S. Yoon, H.S. Lee, J. Mcbreen, Electrochemical and In Situ Synchrotron XRD Studies on Al_2O_3 Coated $LiCoO_2$ Cathode Material, Journal of The Electrochemical Society. 151 (2004).

[43] K.Y. Chung, W.S. Yoon, H.S. Lee, J. Mcbreen, X.Q. Yang, H.O. Si, W.H. Ryu, J.L. Lee, W.I. Cho, B.W. Cho, In situ XRD studies of the structural changes of ZrO_2-coated $LiCoO_2$ during cycling and their effects on capacity retention in lithium batteries, Journal of Power Sources. 163 (2006) 185-190.

[44] W. Lu, J. Zhang, J. Xu, X. Wu, L. Chen, In Situ Visualized Cathode Electrolyte Interphase on $LiCoO_2$ in High Voltage Cycling, Acs Applied Materials & Interfaces. 9 (2017) 19313-19318.

[45] T. Sasaki, Y. Ukyo, Memory effect in a lithium-ion battery, Nat Mater. 12 (2013) 569-575.

[46] H. Kobayashi, M. Hibino, Y. Ogasawara, K. Yamaguchi, T. Kudo, S.I. Okuoka, K. Yonehara, H. Ono, Y. Sumida, M. Oshima, Improved performance of Co-doped Li_2O cathodes for lithium-peroxide batteries using $LiCoO_2$ as a dopant source, Journal of Power Sources. 306 (2016) 567-572.

[47] M. Gauthier, T.J. Carney, A. Grimaud, L. Giordano, N. Pour, H.-H. Chang, D.P. Fenning, S.F. Lux, O. Paschos, C. Bauer, F. Maglia, S. Lupart, P. Lamp, Y. Shao-Horn, Electrode–Electrolyte Interface in Li-Ion Batteries: Current Understanding and New Insights, The Journal of Physical Chemistry Letters. 6 (2015) 4653-4672.

[48] L. Wang, J. Ma, C. Wang, X. Yu, R. Liu, F. Jiang, X. Sun, A. Du, X. Zhou, G. Cui, A Novel Bifunctional Self-Stabilized Strategy Enabling 4.6 V $LiCoO_2$ with Excellent Long-Term Cyclability and High-Rate Capability, Adv Sci (Weinh). 6 (2019) 1900355.

[49] J.L. Tebbe, T.F. Fuerst, C.B. Musgrave, Degradation of Ethylene Carbonate Electrolytes of Lithium Ion Batteries via Ring Opening Activated by $LiCoO_2$ Cathode Surfaces and Electrolyte Species, Acs Appl Mater Interfaces. 8 (2016) 26664-26674.

[50] J.-N. Zhang, Q. Li, Y. Wang, J. Zheng, X. Yu, H. Li, Dynamic evolution of cathode electrolyte interphase (CEI) on high voltage $LiCoO_2$ cathode and its interaction with Li anode, Energy Storage Materials. 14 (2018) 1-7.